NUCL SCI TECH (2020) 31:22
https://doi.org/10.1007/s41365-020-0726-8

Synthesis of a Ag/AgCl/PLA membrane under electron beam irradiation for the photocatalytic degradation of methylene blue and chloramphenicol

Shu-Ting Ji[1] · Qin-Qing Wang[1] · Juan Zhou[1] · Gang Xu[2] · Wen-Yan Shi[1]

Received: 14 August 2019 / Revised: 7 November 2019 / Accepted: 3 December 2019 / Published online: 10 February 2020

Abstract Polylactic acid (PLA) has been extensively applied in the fields of biology and renewable biodegradable materials because of its superior biodegradability. PLA has excellent potential as a renewable biodegradable adsorbent in wastewater treatment. However, its poor photocatalytic properties have hindered its practical application. In this study, polyvinylpyrrolidone (PVPP) or glutaraldehyde (GA) was utilized as an adhesive agent to prepare Ag/AgCl/PLA photocatalysts with highly efficient visible light photocatalysis on a PLA fabric by utilizing the electron beam irradiation method. The photocatalytic activities of the Ag/AgCl/PLA samples were examined under visible light irradiation to analyze the degradation of methylene blue (MB) and chloramphenicol (CPL). Our experimental results demonstrate that the nanomaterial Ag/AgCl was uniformly distributed on the PLA fiber surface; this can be attributed to the effects of the crosslinking PVPP or GA. Under electron beam irradiation, adding crosslinking PVPP (or GA) is beneficial to the loading of Ag/AgCl onto the PLA. For the composite Ag/AgCl/PLA, the degradation rate for MB was as high as 97% after 150 min of visible light irradiation. The addition of 4 mg/ml of Ag/AgCl solution resulted in the greatest photocatalytic activity for CPL, and we advanced the possible degradation pathways of CPL with the best sample. Additionally, the as-prepared composite Ag/AgCl/PLA exhibited favorable antibacterial activity against *E. coli* and *S. aureus*, with a bacterial removal rate of $> 77\%$.

Keywords Ag · AgCl · PLA · Adhesive agent · Electron beam irradiation · Photocatalysis · Antibacterial activity

1 Introduction

Continuous urbanization and industrialization have made environmental pollution a huge challenge for the sustainable development of human society. In recent years, an increasing number of organic pollutants have entered and damaged water systems based on their complex characteristics, slow degradation, and high biological toxicity [1, 2]. Organic dyes and antibiotics are two typical examples of organic pollutants in water. Methylene blue (MB) and chloramphenicol (CPL) are commonly studied as target pollutants. MB is a water-soluble and toxic organic dye that can affect entire ecosystems when it is released into water. It cannot be completely degraded by sunlight [3]. CPL is effective at eliminating Gram-positive and Gram-

This work was supported by the National Natural Science Foundation of China (Nos. 11775138, 11675098, and 41473089), Innovation Program of the Shanghai Municipal Education Commission (No. 13YZ017), and Program for Changjiang Scholars and Innovative Research Teams in Universities (No. IRT13078).

Electronic supplementary material The online version of this article (https://doi.org/10.1007/s41365-020-0726-8) contains supplementary material, which is available to authorized users.

Shu-Ting Ji, Qin-Qing Wang and Juan Zhou have contributed equally to this work.

✉ Gang Xu
xugang@shu.edu.cn

✉ Wen-Yan Shi
wyshi1981@shu.edu.cn

[1] School of Environmental and Chemical Engineering, Shanghai University, Shanghai 200444, China

[2] Shanghai Applied Radiation Institute, Shanghai University, Shanghai 200444, China

negative cocci and bacilli, making it essential for the treatment of human and animal diseases. However, excessive CPL discharge can lead to significant water pollution. It is a more stable pollutant in water than MB and can eventually harm human health [4, 5].

Such dyes and antibiotics pose significant threats to the environment and human beings. Therefore, it has become an important research topic to determine how to remove common organic contaminants from water. As a non-polluting solution that consumes no energy, photocatalytic degradation technology has shown several advantages for wastewater treatment [6–8]. Nanomaterials, such as cuprous oxide (Cu_2O) [9], zinc oxide (ZnO) [10–12], titanium dioxide ($TiO_{2)}$ [13–16], $AuTiO_2$ [17, 18], Au/Cu_2 O [19], Ag/Cu_2O [20], and Ag noble metal photocatalysts, are capable of degrading organic pollutants under visible light. This discovery has attracted significant attention from researchers [21]. Recently, additional attention has been paid to Ag/AgX (X = Cl, Br) surface plasmon photocatalysts. Specifically, a novel method has been developed to expand the visible light absorption of photocatalytic materials based on the plasmon resonance of metal surfaces, which is achieved by combining the surface plasmon resonance effect of noble metals, contact of metal semiconductors, and characteristics of semiconductor photocatalytic materials, thereby promoting the separation of photogenerated electrons in photocatalytic systems [22].

However, some problems regarding the practical applications of nano-silver photocatalysts must be solved, such as the agglomeration of nanoparticle Ag and degradation of substrate materials. To prevent the aggregation of nano-silver photocatalysts in degradation systems, it is necessary to immobilize the photocatalyst on a substrate, such as fabric [23] or plastic [24–26]. Polylactic acid (PLA), which has the advantages of low production cost, no pollution, easy biodegradation, and natural circulation, possesses excellent physical and mechanical properties with a porous structure, which can promote the absorption of contaminants, making it an excellent photocatalyst carrier.

To the best of our knowledge, the preparation of fiber-based Ag/AgCl/PLA has not been reported previously. In this study, polyvinylpyrrolidone (PVPP) and glutaraldehyde (GA) were utilized as crosslinkers to prepare stable Ag/AgCl/PLA composite photocatalytic materials by means of electron beam irradiation. We studied the photocatalytic degradation properties of the as-prepared composites with two common organic compounds (methylene blue (MB) and chloramphenicol (CPL)) as target pollutants. As expected, the Ag/AgCl/PLA composite exhibited better properties for the photocatalytic degradation of MB and CPL compared to pure PLA fibers under visible light irradiation. Additionally, we observed promising antibacterial activity of the Ag/AgCl/PLA composite for pathogenic *E. coli* and *S. aureus*.

2 Experimental

2.1 Chemicals

All the chemicals were analytical grade or better and could be utilized as received without any further purification. $AgNO_3$, GA, and absolute ethanol were purchased from Sinopharm. MB, CPL, polyvinylpyrrolidone (PVPP), glucose, NaCl, and ethylene glycol were purchased from Anpel Laboratory Technologies (Shanghai, China). PLA textiles were provided by Tong Jeliang (Shanghai, China). *E. coli*, *S. aureus*, an inoculating loop, liquid medium, and agar plate were purchased from Guangdong Huan Kai Microbiology Co., Ltd. (Shanghai, China). Ultrapure water produced by a Milli-Q device (18.2 MΩ/cm) was utilized in all experiments.

2.2 Fabrication of Ag/AgCl

Cube-type nano-AgCl was synthesized according to the water-soluble NaCl salt crystal template process [27]. First, 0.544 g of $AgNO_3$ and 2.0 g of PVPP were sequentially dissolved in 100 ml of ethylene glycol solution (glycol/water = 5:1) under ultrasonic treatment and stirred at room temperature (25 °C) for 10 min. Next, 20 ml of 7 mM NaCl aqueous solution was added and stirred for 1 h at room temperature. Finally, 20 ml of 18 mM glucose was added and heated in a water bath at 40 °C for 3 h. The obtained material was then washed with distilled water, a 50% ethanol solution (ethanol/water = 1:1), and absolute ethanol successively three times, followed by sealing in absolute ethanol [28].

2.3 Fabrication of the Ag/AgCl/PLA composite

First, the PLA fibers were cut into pieces that were 4 cm × 4 cm in size and packaged within a custom bag (5 × 5 cm in area) fabricated from polytetrafluoroethylene (PTEF) for subsequent use. Second, 2, 4, and 6 mg/ml of nano-Ag/AgCl and 1 ml of ethanol solution were collected. The crosslinking PVPP or GA was then added, and the obtained solution was injected into the PTEF bag to allow the PLA to be completely saturated by the nano-Ag/AgCl solution. Oxygen was removed through repeated nitrogen blasting, followed by bag sealing. The sealed bag was then irradiated utilizing an electron beam irradiation device at an irradiation dose range of 20–50 kGy. Following this experiment, the composite fiber material was removed

from the bag and vacuum-dried at 60 °C for approximately 6 h to obtain the composite Ag/AgCl/PLA.

2.4 Characterization methods

The sample was characterized utilizing X-ray diffraction (XRD) (Riken Electric Co., Ltd, 18 kw D/MAX2500V+/PC, Japan) with a tube voltage of 40 kV, tube current of 35 MA, scanning range of 2θ = 5–80 °C, and scanning speed of 4 °C/min with a CuKα radiation source (λ = 0.154 nm) [29]. Field-emission scanning electron microscope (SEM) (International Co., Ltd., JSM-7500F, Japan) and energy-dispersive X-ray spectroscopy (EDX) were also employed. The sample surface topography and other features were carefully observed. Additionally, Mg Kα radiation was carried out utilizing X-ray photoelectron spectroscopy (XPS) (Thermofisher Scientific China, Ltd., WSCALAB, UK). Additionally, the structure of the functional groups was observed in a range of 500–4000 cm^{-1} utilizing Fourier transform infrared spectroscopy (FTIR) (Bruker Hongkong Limited, VERTEX 70, Germany). The optical properties of the samples were analyzed utilizing ultraviolet–visible (UV–Vis) spectroscopy and fluorescence spectrophotometry (PL) (PERKINELMER, LS-55, UK).

2.5 Photocatalytic experiments

The adsorption/photocatalytic activities of Ag/AgCl/PLA materials were analyzed based on the degradation of MB and CPL under a 300-W Xe lamp equipped with a 420-nm cutoff filter. In the photocatalytic experiments, Ag/AgCl/ PLA composites with dimensions of 4 cm × 4 cm were added to MB and CPL solutions (50 ml, 10 ppm) and the mixtures were stirred in the dark for 30 min to achieve adsorption equilibrium prior to photoreaction. Next, 2.5 ml of the degraded MB and CPL solutions were sampled every 30 min under visible light irradiation and filtered through a 0.22-μm membrane for further analysis.

2.6 Analysis method

MB absorbance at 664 nm was analyzed by utilizing UV–Vis spectroscopy to investigate the effects of electron beam irradiation dosage on the photodegradation efficiency of the as-prepared samples [30]. To analyze the photodegradation products of CPL utilizing mass spectrometry, we adopted the high-performance liquid chromatograph (HPLC, Agilent 1200LC) method to detect the concentration of CPL. The HPLC column was a Zorbax Eclipse XDB-C18 (4.6 mm (the size of filling material) × 150 mm (innerdiameter), 5 mm (length)), and the detection wavelength was 277 nm. The other test conditions were set based on our previous study [31]. The intermediate products of CPL generated during the degradation process were identified utilizing a quadrupole time-of-flight (Q-TOF) device operating in SCAN mode (electrospray ionization (ESI) (+) and ESI (−)) combined with the HPLC method mentioned above. A solution of formic acid (0.1 vol%, (A)) and methanol (B) was utilized as a mobile phase with an injection volume of 20 μL. The ESI probe tip voltage, capillary potentials, and drying gas flow rate were set to 1 kV, 3.5 kV, and 8L min^{-1}, respectively. The mass range was 50–1200 m/z, and the capillary temperature was set to 40 °C.

2.7 Antibacterial experiments

The prepared nanocomposites were collected for qualitative experiments utilizing *E. coli* and *S. aureus*. For these experiments, all glassware and media solutions were sterilized at 120 °C for 20 min in a stereo autoclave and all experiments were conducted in a sterile environment [22]. First, the composite Ag/AgCl/PLA, nanomaterial Ag/AgCl monomer, and pure PLA were processed into small disks with a diameter of 1 cm, followed by sterilization under a UV lamp on a clean bench for 30 min. Next, 20 μl of diluted bacterial solution was added to the solid medium until the medium surface became smooth and dry. The sterilized materials (Ag/AgCl/PLA, Ag/AgCl monomer, and PLA) were subsequently pressed onto a solid agar nutrition plate utilizing sterile forceps such that the materials were in close contact with the plate. Next, the cells were cultured in a constant-temperature incubator at 37 °C ± 2 °C for 24 h. Each experiment was repeated two times [32].

Quantitative experiments were also performed utilizing the two types of bacteria mentioned above. A diluted bacterial suspension was uniformly mixed into a triangular conical flask containing 60 ml of nutrient medium. The sterile materials (Ag/AgCl/PLA) were then treated with the solution by utilizing sterile forceps. The Ag/AgCl monomer and PLA were placed in a conical flask for spreading and incubated for 24 h on a shaker at a constant temperature (37 °C ± 2 °C, 160 rpm). Each experiment was repeated two times.

3 Results and discussion

3.1 Characterization of the prepared samples

The elemental composition of the nanocomposite Ag/AgCl/PLA was characterized utilizing XPS. Figure 1a presents the full spectrum of the composite Ag/AgCl/PLA with crosslinking PVPP. One can see that the characteristic peaks are largely attributed to Ag3*d*, Cl2*p*, C1*s*, O1*s*, and

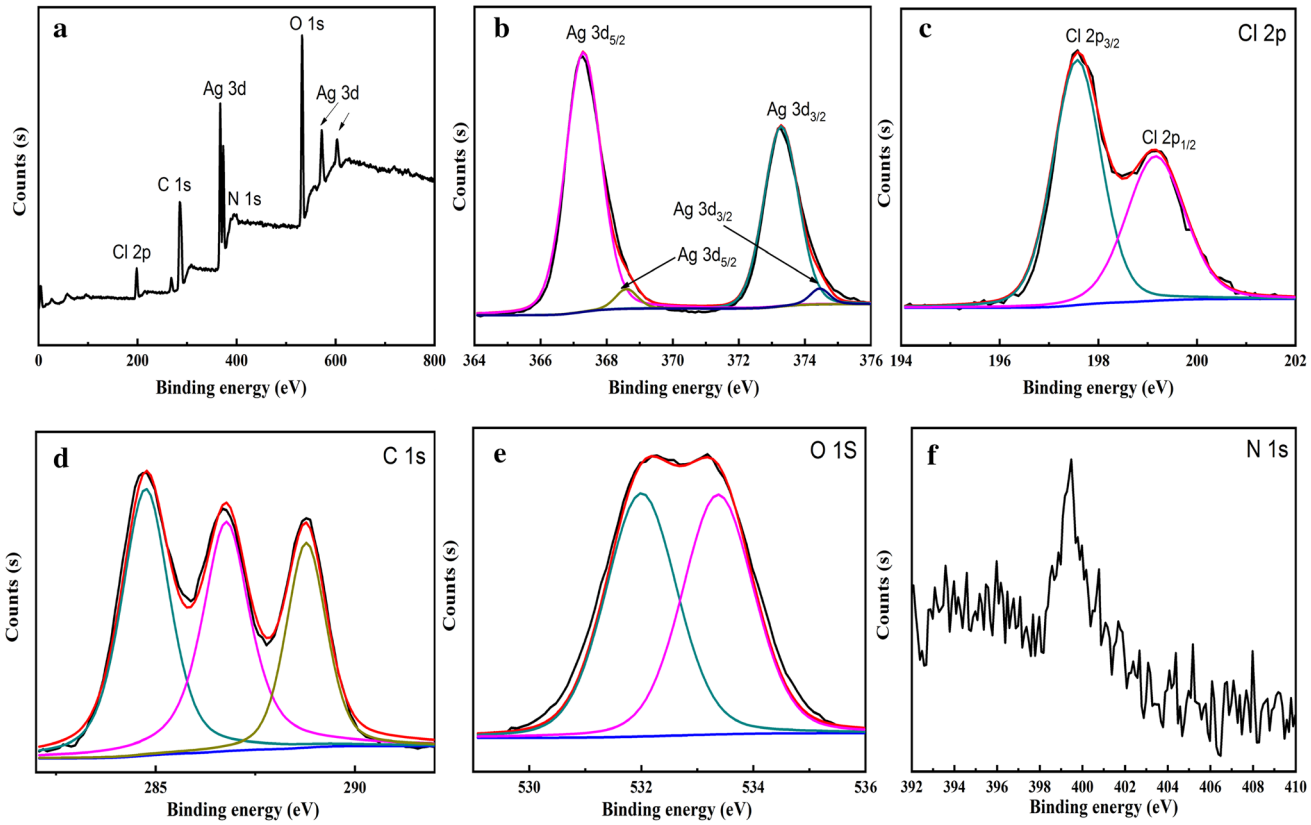

Fig. 1 (Color figure online) XPS spectra of Ag/AgCl/PLA with PVPP nano-frames: **a** survey spectra, **b** Ag3*d*, **c** Cl 2*p*, **d** C 1*s*, **e** O 1*s*, and **f** N 1*s*

N1*s*, where the sources of the Ag and Cl peaks correspond to the prepared sample materials. Additionally, the high-resolution XPS spectrum in Fig. 1b indicates that the characteristic peaks at 367.2 and 373.2 eV correspond to the binding energies of Ag $3d_{5/2}$ and Ag $3d_{3/2}$ orbitals, while those at 368.2 and 374.5 eV correspond to Ag nanoparticles, indicating the presence of zero-valence Ag nanoparticles in the composite. The characteristic peaks at 197.6 and 199.2 eV in the Cl 2*p* high-resolution full spectrum in Fig. 1c can be attributed to the binding energies of the Cl $2p_{3/2}$ and Cl $2p_{1/2}$ orbitals, respectively [33]. Furthermore, the peaks at 284.7, 286.7, and 388.7 eV (Fig. 1d) can be attributed to C [24], while those at 530.8 and 533.7 eV correspond to O (Fig. 1e). When crosslinking GA is added, the nanocomposite Ag/AgCl/PLA is almost identical to that with crosslinking PVPP (Fig. S1). The carbon signal is induced by PLA, PVPP, GA, and indefinite hydrocarbons contained in the XPS instrument itself [34]. The oxygen signal can be attributed to the PLA, PVPP, and GA, while the nitrogen signal comes from the air [35].

The PLA surface was smooth with fiber widths of approximately 15,000 nm, as shown in Fig. 2a. In Fig. 2b, the nano-Ag/AgCl exhibits a regular cubic structure with particle sizes in the range of approximately 100–200 nm. Smaller silver nanoparticles (< 100 nm) can be observed on the tops of the AgCl cubes. In Fig. 2c, d, a large amount of cubic crystal nanomaterial Ag/AgCl is evenly bonded onto the PLA surfaces following the electron beam irradiation at 40 kGy. The binders are also combined, indicating that the nanomaterial Ag/AgCl and crosslinking PVPP and GA are successfully connected to the PLA surface. EDX spectra of PLA coated with Ag/AgCl and GA and with Ag/AgCl and PVPP are presented in Fig. 2e, f, respectively. One can clearly see the presence of C, O, Ag, and Cl in the composites. According to Table 1, the atomic ratios of Ag to Cl are 1.3:1 and 2.1:1 in the two composites, respectively, indicating the presence of Ag in Ag/AgCl nanojunction systems [36].

The crystalline structures of PLA, Ag/AgCl, Ag/AgCl/PLA containing PVPP and Ag/AgCl/PLA containing GA were utilizing XRD (Fig. 3a). One can see that the PLA retains diffraction peaks at approximately $2\theta = 16.79°$, which can be attributed to the PLA itself [37]. The characteristic diffraction peaks of Ag/AgCl/PLA containing PVPP and Ag/AgCl/PLA containing GA at $2\theta = 28.0°$, 32.4°, 46.4°, 54.9°, 57.6°, and 67.5° correspond to the cubic AgCl (111), (200), (220), (311), (222), and (400) planes, respectively [38]. These results indicate that the nanomaterial Ag/AgCl was successfully attached to the PLA surface by means of electron beam irradiation and that

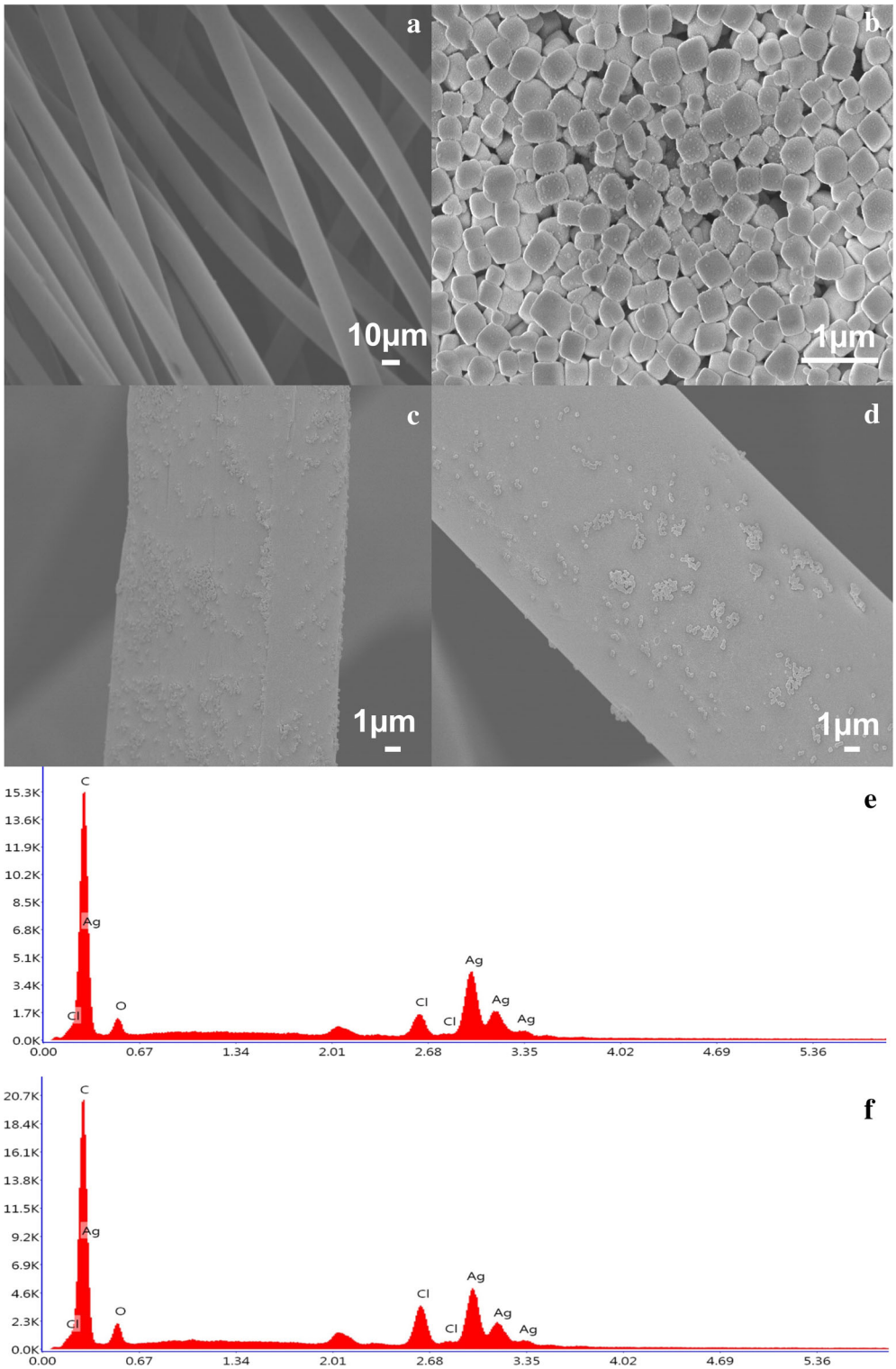

Fig. 2 (Color figure online) SEM images of **a** PLA, **b** Ag/AgCl, **c** Ag/AgCl/PLA with GA, and **d** PVPP, and corresponding EDX spectra of Ag/AgCl/PLA with **e** GA and **f** PVPP

the crosslinkers were successfully adhered. However, a significant nano-Ag characteristic peak cannot be observed in the XRD spectra of Ag/AgCl and PLA, which can be attributed to the small nano-Ag size and low deposition content of Ag on the PLA surface [25, 39].

Table 1 Major element contents of the composite photocatalytic materials

	Major element (content, mass%)			
	C	O	Ag	Cl
Ag/AgCl/PLA with GA	77.57	9.12	7.58	5.72
Ag/AgCl/PLA with PVPP	75.77	9.64	9.83	4.75

Figure 3b presents the UV–Vis diffuse reflectance spectrum of the composite Ag/AgCl/PLA. One can see that the absorption edge of the pure PLA is located at approximately 405 nm, while the light absorption edge of the composite Ag/AgCl/PLA exhibits a slight red shift. The light absorption edge of the pure Ag/AgCl nanoparticles is located at approximately 410 nm, which corresponds to the band gap of AgCl (3.2 eV). The light absorption capacity of the Ag/AgCl/PLA composites is slightly enhanced in the ultraviolet and visible regions after they are deposited, which can be attributed to the surface plasmon resonance effect of the Ag species formed on the original AgCl nanoparticle surfaces, implying that loading Ag/AgCl nanoparticles onto PLA fibers can facilitate the utilization of visible light.

Figure 3c presents the fluorescence spectra of PLA, nanomaterial Ag/AgCl, and composite Ag/AgCl/PLA. One can see that the pure PLA exhibits the strongest fluorescence emission peak, while that of the composite is relatively weak, which could be a result of the electron trapping effect of Ag, which could lead to the deposition of Ag/AgCl nanoparticles on the PLA, significantly inhibiting the recombination of photoexcited electron–hole pairs.

The chemical interactions between Ag/AgCl and the PLA fabric surface were investigated utilizing FTIR (Fig. 3d). Figure 3d presents the FTIR spectra of PLA and composite Ag/AgCl/PLA in a spectral range of

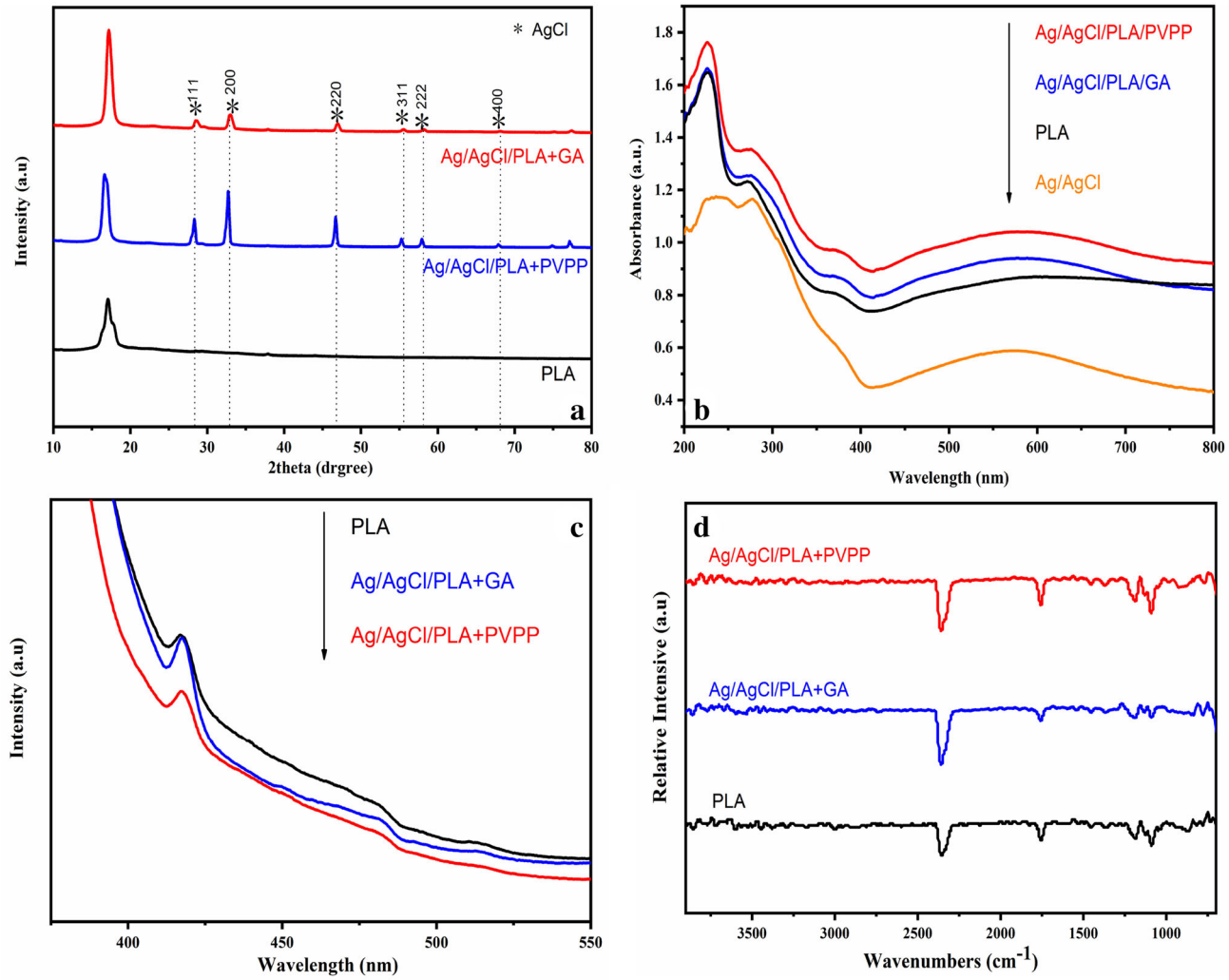

Fig. 3 (Color figure online) **a** XRD, **b** UV–vis, **c** PL, and **d** FTIR characterization of Ag/AgCl/PLA with PVPP, Ag/AgCl/PLA with GA, and PLA

3500–100 cm^{-1}. Typically, an absorption peak at 2750 cm^{-1} is attributed to the stretching vibrations of O–H groups, which are generated by the deformation vibrations of PLA-absorbed water molecules [37]. The infrared spectra of the composite Ag/AgCl/PLA and PLA were compared and analyzed, and it was determined that the composite Ag/AgCl/PLA exhibits a characteristic absorption peak of –C=O– at 1250 cm^{-1}, which was not observed for the pure PLA. We believe that both ethanol and PLA can generate free –C=O– under high-energy electron beam irradiation. As a result, the composite should experience peak-shaped splitting for –C=O– (1250 cm^{-1}). Additionally, a very small absorption peak could be considered as an acceptor for hydrogen bonds to form hydroxyl groups (–OH), where the crosslinkers on the nano-Ag/AgCl surfaces act as hydrogen bond donors. Specifically, hydrogen bonds indicate chemical interactions between Ag/AgCl and PLA following the addition of crosslinkers.

3.2 Photocatalytic experiments

Table 2 lists the nanomaterials loaded onto PLA with 1% GA and 10 mg of PVPP content under different nanomaterial Ag/AgCl and electron beam irradiation doses. According to these results, when 4 mg/ml of nano-Ag/AgCl solution is added and the electron beam irradiation dose is 40 kGy, the amount of nanomaterial Ag/AgCl loaded onto the PLA surface reaches 2.9 mg (1% GA) and 3.2 mg (10 mg PVPP). For single-variable analysis, we utilized MB as a target pollutant to determine the effect of irradiation dose on the photocatalytic degradation of Ag/AgCl/PLA with GA and PVPP (Fig. 4). Overall, the photocatalytic performance of the materials increases initially and then decreases with increasing irradiation doses. The "40 kGy-GA" sample exhibits the highest photocatalytic activity with an MB degradation rate as high as 96.98% over 150 min, which is superior to the values for the 0 kGy-GA (75.76%), 30 kGy-GA (89.27%), and 50 kGy-GA (87.54%) samples. The similar results can be observed in Fig. 4b. This is because high-dose electron beams have a negative effect on the grafting reactions between Ag/AgCl and PLA and may even damage original grafting chains. Additionally, the ratio of activation of the Ag/AgCl monomer increases so rapidly at high doses that the probability of agglomeration among monomers increases [40].

Table 2 Results when crosslinking GA (1%) and PVPP (10 mg) are loaded onto the PLA surface via electron beam irradiation with different irradiation doses and nanomaterial Ag/AgCl contents

Crosslinker	Irradiation dose (kGy)	Nanomaterial contents (mg)		
		2 mg/ml	4 mg/ml	6 mg/ml
GA	0	1	1.6	2
	30	1.1	2.4	2.5
	40	1.2	2.9	2.7
	50	1.4	2.8	2.6
PVPP	0	1	1.6	2
	30	1.4	2.8	3
	40	1.4	3.2	3.1
	50	1.5	3	2.9

The materials obtained under optimal conditions were analyzed to compare photocatalytic properties among the pure PLA fiber, Ag/AgCl/PLA containing PVPP and Ag/AgCl/PLA containing GA based on photocatalytic degradation experiments (Fig. 5). The degradation efficiency of the pure PLA fiber for MB was only approximately 41% after 150 min of irradiation under visible light. A portion of this value can be attributed to the photodegradation of MB itself (Fig. 5). These results indicate that PLA fiber has a very weak photocatalytic effect in terms of removing MB and only provides photo-adsorption during the photocatalytic process, thereby accelerating the photocatalytic degradation process. In contrast, under the same conditions, the Ag/AgCl/PLA composite system exhibits higher photocatalytic activity with a photocatalytic efficiency of 84%. The photocatalytic activity of the Ag/AgCl/PLA with GA composite system is 96% and that of the Ag/AgCl/PLA with PVPP system is 97%. This is because the crosslinking agents can increase Ag/AgCl loading in the PLA, resulting in enhanced photocatalytic performance.

CPL is a colorless organic compound that is more stable than MB under visible light. Therefore, CPL was selected as a target for studying the effects of Ag/AgCl addition on photocatalytic degradation based on the optimal irradiation dose. Figure 6a reveals that when the nano-Ag/AgCl content is 4 mg/ml, 100% degradation occurs after 120 min for Ag/AgCl/PLA with GA. The similar results can be observed for Ag/AgCl/PLA with PVPP, as shown in Fig. 6b. Clearly, the addition of 4 mg/ml of nano-Ag/AgCl contributes to the desirable particle dispersion of Ag/AgCl, which effectively prevents the nanomaterials from obstructing the surface active substances of the composites based on clustering, resulting in additional photogenerated electron–hole pairs for the photocatalytic process [41, 42].

Figure 7 compares the XRD patterns of composites before and after photoreaction in the range of 20–80° (2θ). Characteristic peaks at 38.1° and 44.2°, which are attributed to the (111) and (200) planes of metallic Ag [43], can be observed after photoreaction (b, d). This indicates that AgCl may decompose into a small amount of silver and bromine atoms during the photoreaction process based on its high sensitivity to light. Additionally, the

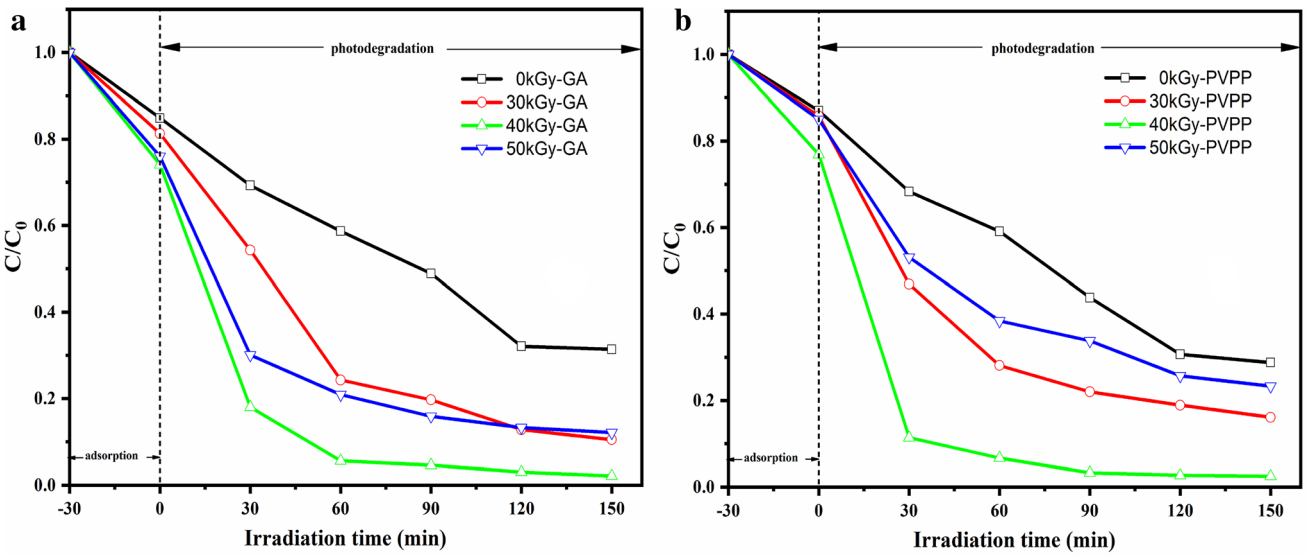

Fig. 4 (Color figure online) Degradation of MB by Ag/AgCl/PLA with **a** GA and **b** PVPP crosslinkers at different irradiation doses (C_0 is concentration of adsorption equilibrium prior to the photocatalytic experiments)

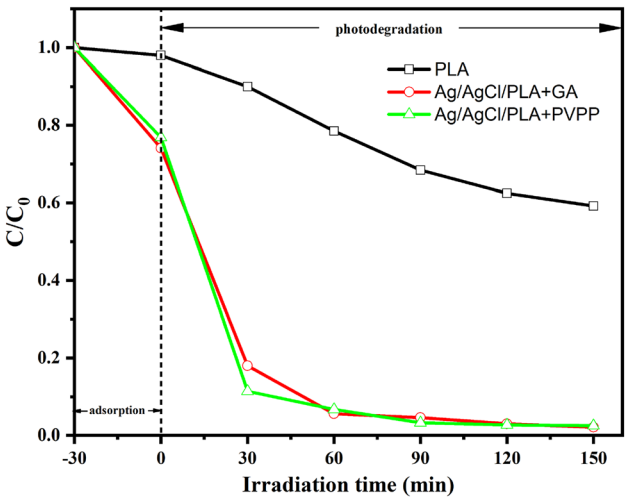

Fig. 5 (Color figure online) Photocatalytic performance of pure PLA, Ag/AgCl/PLA with GA, and Ag/AgCl/PLA with PVPP for the decomposition of MB under visible light irradiation ($\lambda > 420$ nm)

photogenerated carriers reduce the partial Ag^+ ions produced by AgCl into Ag^0 by preventing additional light corrosion of AgCl under xenon lamp irradiation [44]. However, the positions of the other peaks change very little. These results indicate that the composites have sufficient stability to support efficient photocatalytic reactions.

3.3 Proposed reaction pathways

The intermediate products resulting from photocatalytic degradation of CPL by the 40 kGy-GA 4 mg/ml and 40 kGy-PVPP 4 mg/ml samples at 30, 60, 90, 120, and 150 min were analyzed. According to the mass spectra of the photocatalytic degradation of CPL at different reaction times (Fig. S2), the CPL disappears after 120 min, which is consistent with the HPLC findings. Figure 8 presents the proposed photocatalytic degradation pathways of CPL, including radical reaction, ring opening, oxidation, substitution, and decarboxylation, which were obtained via liquid chromatography–mass spectrometry (Q-TOF) detection [45]. The degradation of CPL begins with the cleavage of C–Cl and C–N bonds to form p1 and p18, which are further hydroxylated or dehydrated into p2 and p19, respectively. Breakage of the lateral chain of CPL via hydroxylation of C–N bonds leads to the formation of p3 at 30 min. Additionally, C–OH structures and the products of amino groups in the branch chains of CPL can be easily oxidized into C=O structures under photocatalytic conditions, leading to the formation of p4, p5, p7, and p11. Next, p12 and p15 are generated via denitrification and dehalogenation after 60 min of reaction, followed by oxidation and fracturing to produce a series of products (p13, p14, p16, p17) [46]. Additionally, CPL is disintegrated via dechloridation under hydroxyl radical attacks to produce p8 and p9. Deprotonated products, such as p6 and p10, are formed via further hydroxylation of p4 and p9. Ring opening products may eventually appear after 150 min [47].

3.4 Antibacterial activity

The results of antibacterial experiments on PLA, nanomaterial Ag/AgCl, and composite Ag/AgCl/PLA are presented in Fig. 9. One can see that pure PLA has no clear antibacterial zone for *E. coli* and *S. aureus*, unlike the composite material Ag/AgCl/PLA with PVPP, which has a

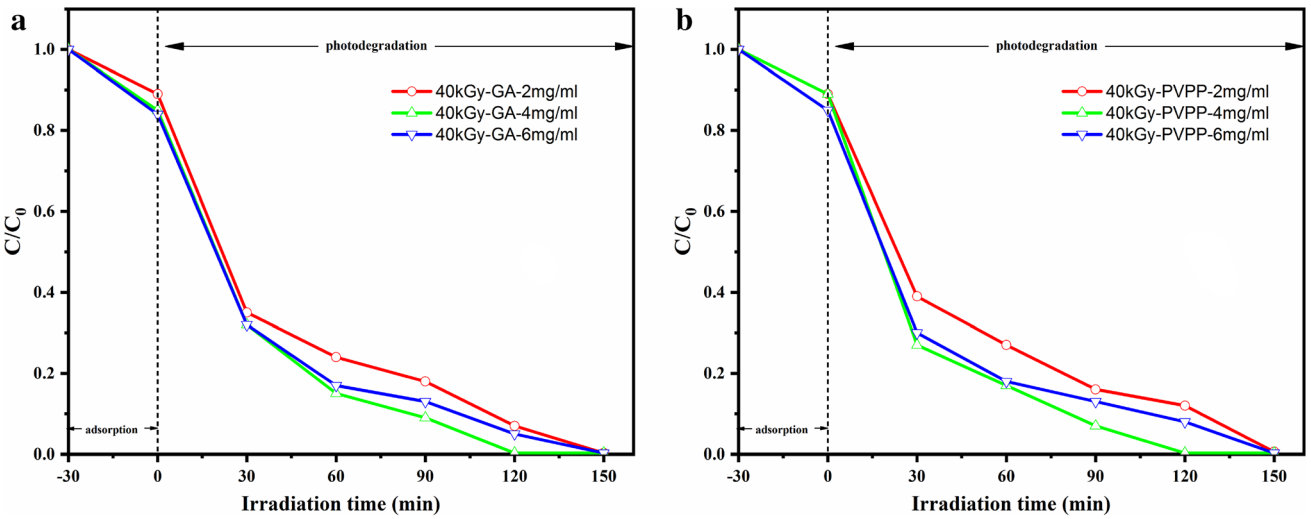

Fig. 6 (Color figure online) Relationship between the photocatalytic activity of CPL and loading amount of Ag/AgCl/PLA with **a** GA and **b** PVPP under visible light irradiation (C_0 is concentration of adsorption equilibrium prior to the photocatalytic experiments)

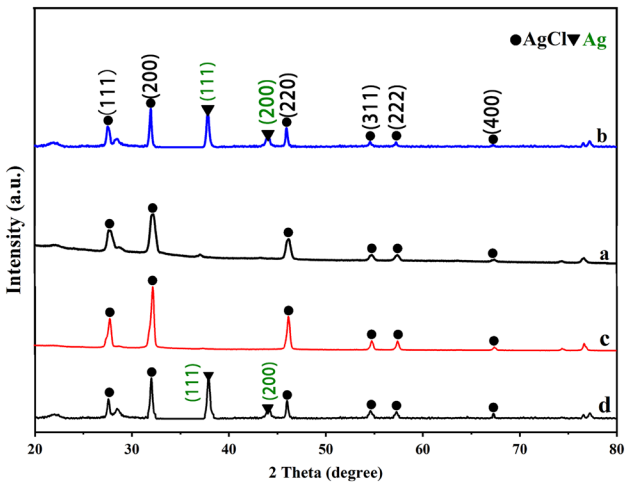

Fig. 7 (Color figure online) XRD patterns of Ag/AgCl/PLA with GA **a** before and **b** after photocatalytic reaction and Ag/AgCl/PLA with PVPP **c** before and **d** after photocatalytic reaction

bacteriostatic range of 15 mm. The composite material Ag/AgCl/PLA with GA has an inhibition zone of approximately 16 mm. These results indicate that pure PLA has no significant antibacterial ability, but the composite Ag/AgCl/PLA does have significant antibacterial ability [48]. Although the antimicrobial mechanism of Ag/AgCl has not been defined clearly, the free radicals produced by photocatalysis have clear bactericidal effects [49]. As indicated by the results discussed above, the composite material containing crosslinking GA has a larger antibacterial ring compared to the composite material containing PVPP. We suspected that the GA itself provided antibacterial effects, so another set of experiments were conducted by adding GA to the pure PLA. The results indicated no obvious inhibition zone. Such results could be related to the relatively small amount of GA, which may have no obvious bacteriostatic effects.

To investigate the inhibition rates of different materials on *E. coli* and *S. aureus*, quantitative experiments were conducted on different materials. The experimental results are presented in Fig. 10. As shown in Fig. 10, the inhibition rates of pure PLA for *E. coli* and *S. aureus* are only 1.64%, which are almost negligible. The inhibition rates of the Ag/AgCl for *E. coli* and *S. aureus* are 56.56% and 55.68%, respectively. The inhibition rates of the Ag/AgCl/PLA with PVPP for E. coli and S. aureus are 77.55% and 77.79%, respectively. The inhibition rates of the Ag/AgCl/PLA with GA for *E. coli* and *S. aureus* are 82.66% and 82.36%, respectively. As shown by the bacteriostatic results, the bacteriostatic effect of the monomer is much weaker than that of the composite materials, which could be because the presence of PLA allows the nanomaterial Ag/AgCl to contact more bacteria, resulting in a significant antibacterial effect. Additionally, a set of controlled experiments was conducted on GA and PLA to confirm the hypothesis discussed above. The results in Fig. 9 reveal that the inhibition rate of GA is approximately 10%, which is consistent with our hypothesis, indicating that GA is bacteriostatic against *E. coli* and *S. aureus*.

4 Conclusion

Ag/AgCl/PLA composites containing PVPP or GA crosslinkers were successfully prepared by means of electron beam irradiation. According to the single-control-variable method, the optimal irradiation dose was determined based on the photodegradation of MB. We then studied the effects of Ag/AgCl addition on the

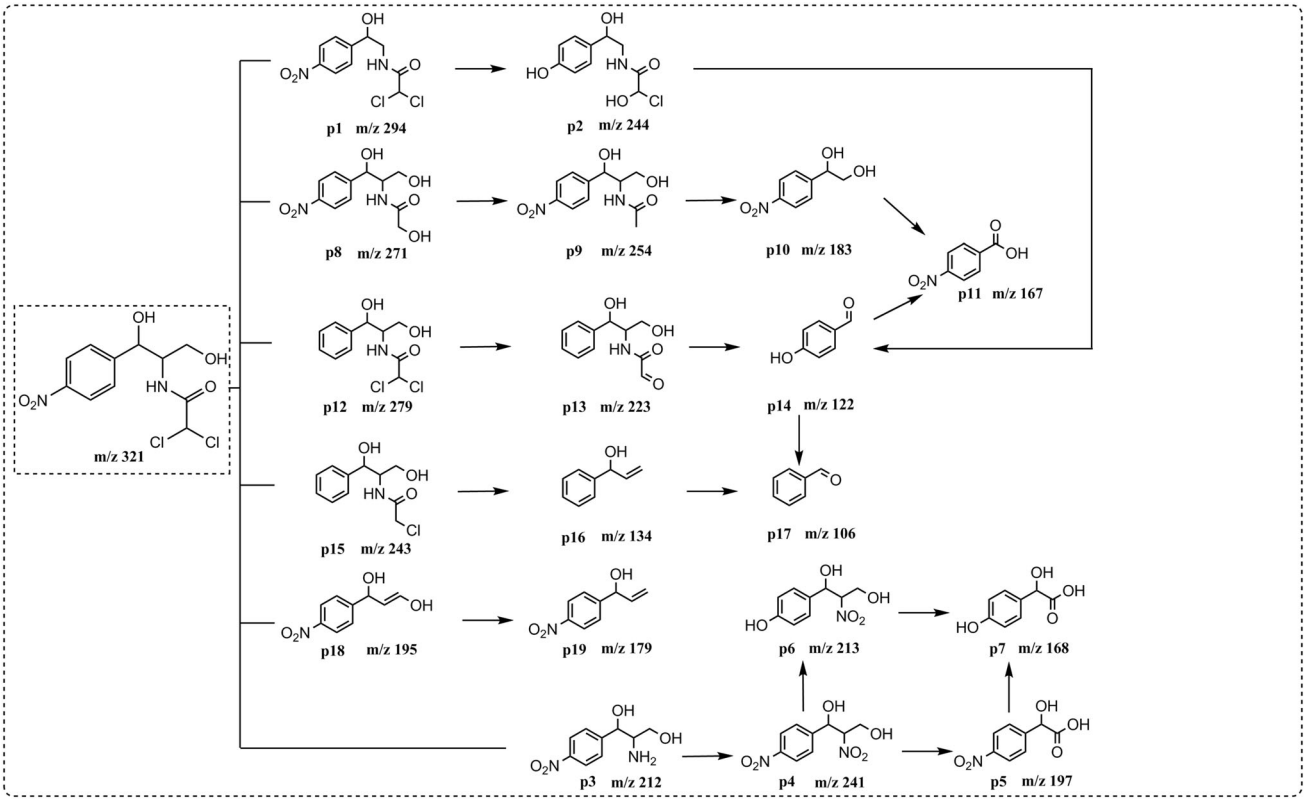

Fig. 8 Proposed photocatalytic degradation pathways of CPL

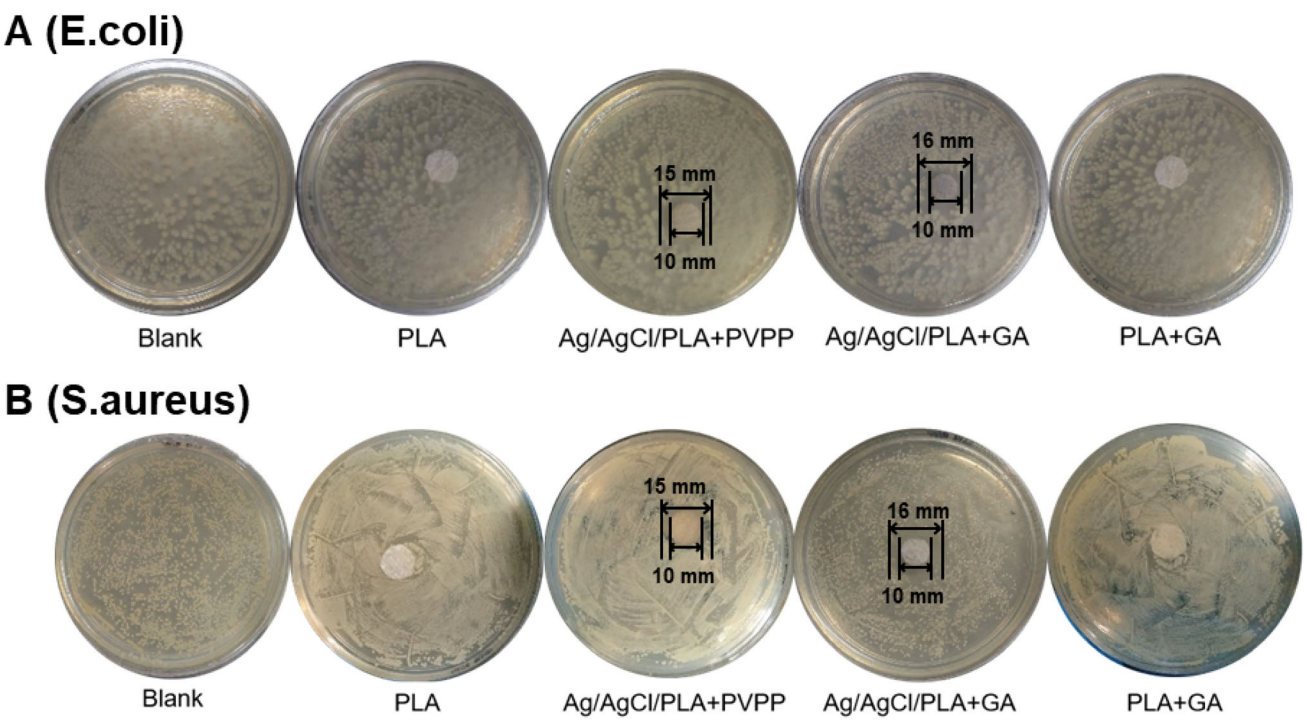

Fig. 9 Comparative antibacterial activities against *E. coli* and *S. aureus* for PLA, Ag/AgCl/PLA with PVPP, Ag/AgCl/PLA with GA, and PLA with GA

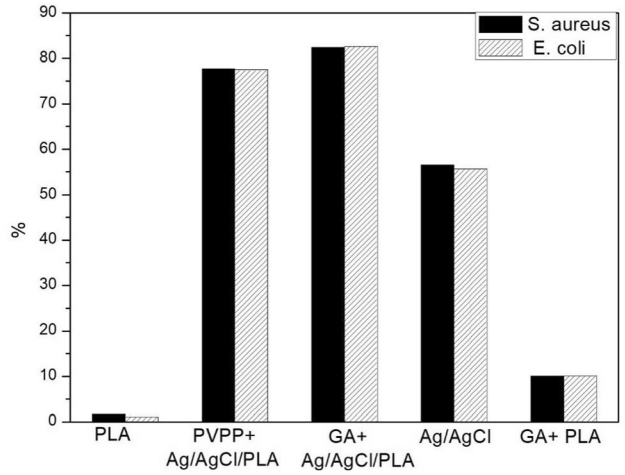

Fig. 10 Comparative antibacterial rates against the *E. coli* and *S. aureus* for PLA, Ag/AgCl/PLA with PVPP, Ag/AgCl/PLA with GA, Ag/AgCl, and PLA with GA

photocatalytic properties of optimized samples. The composites exhibited excellent photocatalytic performance for both MB and CPL under optimal conditions. Additionally, the Ag/AgCl/PLA composites exhibited significant antibacterial ability with inhibition rates as high as 77%. All these results indicate that such composites are effective for the treatment of complex and refractory organic wastewater. Therefore, it is of critical importance to investigate the practical application of the composite material Ag/AgCl/PLA.

References

1. Z. Song, Y.Q. He, Novel AgCl/Ag/$AgFeO_2$ Z-scheme heterostructure photocatalyst with enhanced photocatalytic and stability under visible light. Appl. Surf. Sci. **420**, 911–918 (2017). https://doi.org/10.1016/j.apsusc.2017.05.212
2. M. Mousavi, A. Habibi-Yangjeh, S.R. Pouran, Review on magnetically separable graphitic carbon nitride-based nanocomposites as promising visible-light-driven photocatalysts. J. Mater. Sci. Mater. Electron. **29**(3), 1719–1747 (2017). https://doi.org/10.1007/s10854-017-8166-x
3. R.J. Tayade, T.S. Natarajan, H.C. Bajaj, Photocatalytic degradation of methylene blue dye using ultraviolet light emitting diodes. Ind. Eng. Chem. Res. **48**, 10262–10267 (2009). https://doi.org/10.1021/ie9012437
4. C.Q. Tan, Y.J. Dong, D.F. Fu et al., Chloramphenicol removal by zero valent iron activated peroxymonosulfate system: kinetics and mechanism of radical generation. Chem. Eng. J. **334**, 1006–1015 (2018). https://doi.org/10.1016/j.cej.2017.10.020
5. S.Q. Xia, Z.L. Gu, Z.Q. Zhang et al., Removal of chloramphenicol from aqueous solution by nanoscale zero-valent iron particles. Chem. Eng. J. **257**, 98–104 (2014). https://doi.org/10.1016/j.cej.2014.06.106
6. Y.Y. Fan, W.G. Ma, D.G. Han et al., Convenient recycling of 3D AgX/graphene aerogels (X = Br, Cl) for efficient photocatalytic degradation of water pollutants. Adv. Mater. **27**(25), 3767–3773 (2015). https://doi.org/10.1002/adma.201500391
7. M.N. Chong, B. Jin, C.W. Chow et al., Recent developments in photocatalytic water treatment technology: a review. Water Res. **44**(10), 2997–3027 (2010). https://doi.org/10.1016/j.watres.2010.02.039
8. D.J. Martin, G.G. Liu, S.J. Moniz et al., Efficient visible driven photocatalyst, silver phosphate: performance, understanding and perspective. Chem. Soc. Rev. **44**(21), 7808–7828 (2015). https://doi.org/10.1039/c5cs00380f
9. M. Hara, T. Kondo, M. Komoda et al., Cu_2O as a photocatalyst for overall water splitting under visible light irradiation. Chem. Commun. **3**, 357–358 (1998). https://doi.org/10.1039/a707440i
10. D.L. Shao, J. Gao, G.Q. Xin et al., Cl-doped ZnO nanowire arrays on 3D graphene foam with highly efficient field emission and photocatalytic properties. Small **11**(36), 4785–4792 (2015). https://doi.org/10.1002/smll.201501411
11. S.K. Le, T.S. Jiang, Y.W. Li et al., Highly efficient visible-light-driven mesoporous graphitic carbon nitride/ZnO nanocomposite photocatalysts. Appl. Catal. B **200**, 601–610 (2017). https://doi.org/10.1016/j.apcatb.2016.07.027
12. V. Vaiano, G. Iervolino, L. Rizzo, Cu-doped ZnO as efficient photocatalyst for the oxidation of arsenite to arsenate under visible light. Appl. Catal. B **238**, 471–479 (2018). https://doi.org/10.1016/j.apcatb.2018.07.026
13. J. Schneider, M. Matsuoka, M. Takeuchi et al., Understanding TiO_2 photocatalysis: mechanisms and materials. Chem. Rev. **114**(19), 9919–9986 (2014). https://doi.org/10.1021/cr5001892
14. K.P.O. Mahesh, D.H. Kuo, B.R. Huang et al., Chemically modified polyurethane-SiO_2/TiO_2 hybrid composite film and its reusability for photocatalytic degradation of Acid Black 1 (AB 1) under UV light. Appl. Catal. A **475**, 235–241 (2014). https://doi.org/10.1016/j.apcata.2014.01.044
15. W.A. Thompson, C. Perier, M.M. Maroto-Valer, Systematic study of sol-gel parameters on TiO_2 coating for CO_2 photoreduction. Appl. Catal. B **238**, 136–146 (2018). https://doi.org/10.1016/j.apcatb.2018.07.018
16. A. Ziarati, A. Badiei, R. Luque, Black hollow TiO_2 nanocubes: advanced nanoarchitectures for efficient visible light photocatalytic applications. Appl. Catal. B **238**, 177–183 (2018). https://doi.org/10.1016/j.apcatb.2018.07.020
17. M. Abid, S. Bouattour, A.M. Ferraria et al., Functionalization of cotton fabrics with plasmonic photo-active nanostructured Au-TiO_2 layer. Carbohydr. Polym. **176**, 336–344 (2017). https://doi.org/10.1016/j.carbpol.2017.08.090
18. G. Yang, H. Ding, D. Chen et al., Construction of urchin-like $ZnIn_2S_4$-Au-TiO_2 heterostructure with enhanced activity for photocatalytic hydrogen evolution. Appl. Catal. B **234**, 260–267 (2018). https://doi.org/10.1016/j.apcatb.2018.04.038
19. C.H. Kuo, Y.C. Yang, S. Gwo et al., Facet-dependent and au nanocrystal-enhanced electrical and photocatalytic properties of Au-Cu_2O core-shell heterostructures. J. Am. Chem. Soc. **133**(4), 1052–1057 (2011). https://doi.org/10.1021/ja109182y
20. W.L. Li, J.J. Wang, H.X. Chi et al., Preparation and antibacterial activity of polyvinyl alcohol/regenerated silk fibroin composite fibers containing Ag nanoparticles. J. Appl. Polym. Sci. **123**(1), 20–25 (2012). https://doi.org/10.1002/app.34434
21. P. Wang, B.B. Huang, X.Y. Qin et al., Ag@AgCl: a highly efficient and stable photocatalyst active under visible light. Angew. Chem. Int. Ed. Engl. **47**(41), 7931–7933 (2008). https://doi.org/10.1002/anie.200802483
22. Q.Q. Liu, Y.G. Xu, J. Wang et al., Fabrication of Ag/AgCl/$ZnFe_2O_4$ composites with enhanced photocatalytic activity for pollutant degradation and *E. coli* disinfection. Colloids Surf. A **553**, 114–124 (2018). https://doi.org/10.1016/j.colsurfa.2018.05.019

23. S.A. Mao, R. Bao, D. Fang et al., Facile synthesis of Ag/AgX (X = Cl, Br) with enhanced visible-light-induced photocatalytic activity by ultrasonic spray pyrolysis method. Adv. Powder Technol. **29**(11), 2670–2677 (2018). https://doi.org/10.1016/j.apt.2018.07.016
24. S.W. Zhang, J.X. Li, X.K. Wang et al., In situ ion exchange synthesis of strongly coupled Ag@AgCl/g-C(3)N(4) porous nanosheets as plasmonic photocatalyst for highly efficient visible-light photocatalysis. ACS Appl. Mat. Interfaces **6**(24), 22116–22125 (2014). https://doi.org/10.1021/am505528c
25. W.D. Zhang, X.A. Dong, Y. Liang et al., Ag/AgCl nanoparticles assembled on BiOCl/$Bi_{12}O_{17}C_{l2}$ nanosheets: enhanced plasmonic visible light photocatalysis and in situ DRIFTS investigation. Appl. Surf. Sci. **455**, 236–243 (2018). https://doi.org/10.1016/j.apsusc.2018.05.171
26. X. Lv, T.H. Wang, W. Jiang, Preparation of Ag@AgCl/g-C_3N_4/TiO_2 porous ceramic films with enhanced photocatalysis performance and self-cleaning effect. Ceram. Int. **44**(8), 9326–9337 (2018). https://doi.org/10.1016/j.ceramint.2018.02.145
27. X.L. Xiao, L. Ge, C.C. Han et al., A facile way to synthesize Ag@AgBr cubic cages with efficient visible-light-induced photocatalytic activity. Appl. Catal. B **163**, 564–572 (2015). https://doi.org/10.1016/j.apcatb.2014.08.037
28. G.D. Fan, X. Zheng, J. Luo et al., Rapid synthesis of Ag/AgCl@ZIF-8 as a highly efficient photocatalyst for degradation of acetaminophen under visible light. Chem. Eng. J. **351**, 782–790 (2018). https://doi.org/10.1016/j.cej.2018.06.119
29. C.C. Han, L. Ge, C.F. Chen et al., Site-selected synthesis of novel Ag@AgCl nanoframes with efficient visible light induced photocatalytic activity. J. Mater. Chem. A **2**(31), 12594–12600 (2014). https://doi.org/10.1039/c4ta01941e
30. S. Zhao, Y.W. Zhang, Y.M. Zhou et al., Reactable polyelectrolyte-assisted preparation of flower-like Ag/AgCl/BiOCl composite with enhanced photocatalytic activity. J. Photochem. Photobiol. A **350**, 94–102 (2018). https://doi.org/10.1016/j.jphotochem.2017.09.070
31. Q. Xu, Z.J. Song, S.T. Ji et al., The photocatalytic degradation of chloramphenicol with electrospun $Bi_2O_2CO_3$-poly(ethylene oxide) nanofibers: the synthesis of crosslinked polymer, degradation kinetics, mechanism and cytotoxicity. RSC Adv. **9**(51), 29917–29926 (2019). https://doi.org/10.1039/c9ra06346c
32. L.H. Dong, D.D. Liang, R.C. Gong, In situ photoactivated AgCl/Ag nanocomposites with enhanced visible light photocatalytic and antibacterial activity. Eur. J. Inorg. Chem. **2012**(19), 3200–3208 (2012). https://doi.org/10.1002/ejic.201200172
33. J. Yan, H. Xu, Y.G. Xu et al., Synthesis, characterization and photocatalytic activity of Ag/AgCl/graphite-like C_3N_4 under visible light irradiation. J. Nanosci. Nanotechnol. **14**(9), 6809–6815 (2014). https://doi.org/10.1166/jnn.2014.8975
34. Y.B. Du, C.G. Niu, L. Zhang et al., Synthesis of Ag/AgCl hollow spheres based on the Cu_2O nanospheres as template and their excellent photocatalytic property. Mol. Catal. **436**, 100–110 (2017). https://doi.org/10.1016/j.mcat.2017.03.022
35. B.V.R. Chowdari, P.P. Kumari, Structure and ionic conduction in the $Ag_2O{\cdot}WO_3{\cdot}TeO_2$ glass system. J. Mater. Sci. **33**, 3591–3599 (1998). https://doi.org/10.1023/A:1004651228203
36. Y.H. Liang, S.L. Lin, L. Liu et al., Oil-in-water self-assembled Ag@AgCl QDs sensitized Bi_2WO_6: enhanced photocatalytic degradation under visible light irradiation. Appl. Catal. B **164**, 192–203 (2015). https://doi.org/10.1016/j.apcatb.2014.08.048
37. S. Hu, P. Li, Z. Wei et al., Antimicrobial activity of nisin-coated polylactic acid film facilitated by cold plasma treatment. J. Appl. Polym. Sci. **135**(47), 46844 (2018). https://doi.org/10.1002/app.46844
38. W.J. Ong, L.K. Putri, L.L. Tan et al., Heterostructured AgX/g-C_3N_4 (X = Cl and Br) nanocomposites via a sonication-assisted deposition-precipitation approach: emerging role of halide ions in the synergistic photocatalytic reduction of carbon dioxide. Appl. Catal. B **180**, 530–543 (2016). https://doi.org/10.1016/j.apcatb.2015.06.053
39. Q. Yang, M. Hu, J. Guo et al., Synthesis and enhanced photocatalytic performance of Ag/AgCl/TiO_2 nanocomposites prepared by ion exchange method. J. Materiomics **4**(4), 402–411 (2018). https://doi.org/10.1016/j.jmat.2018.06.002
40. L. Wang, P.X. Jin, S.H. Duan et al., In-situ incorporation of Copper(II) porphyrin functionalized zirconium MOF and TiO_2 for efficient photocatalytic CO_2 reduction. Sci. Bull. **64**(13), 926–933 (2019). https://doi.org/10.1016/j.scib.2019.05.012
41. G. Liu, G.H. Wang, Z.H. Hu et al., Ag_2O nanoparticles decorated TiO_2 nanofibers as a p-n heterojunction for enhanced photocatalytic decomposition of RhB under visible light irradiation. Appl. Surf. Sci. **465**, 902–910 (2019). https://doi.org/10.1016/j.apsusc.2018.09.216
42. L. Liu, L. Ding, Y.G. Liu et al., Enhanced visible light photocatalytic activity by Cu_2O-coupled flower-like Bi_2WO_6 structures. Appl. Surf. Sci. **364**, 505–515 (2016). https://doi.org/10.1016/j.apsusc.2015.12.170
43. L. Liu, S.L. Lin, J.S. Hu et al., Plasmon-enhanced photocatalytic properties of nano Ag@AgBr on single-crystalline octahedral Cu2O (1 1 1) microcrystals composite photocatalyst. Appl. Surf. Sci. **330**, 94–103 (2015). https://doi.org/10.1016/j.apsusc.2015.01.021
44. P. Tun, K. Wang, H. Naing et al., Facile preparation of visible-light-responsive kaolin-supported Ag@AgBr composites and their enhanced photocatalytic properties. Appl. Clay Sci. **175**, 76–85 (2019). https://doi.org/10.1016/j.clay.2019.04.003
45. Y.S. Zhang, Y.S. Shao, N.Y. Gao et al., Kinetics and by-products formation of chloramphenicol (CAP) using chlorination and photocatalytic oxidation. Chem. Eng. J. **333**, 85–91 (2018). https://doi.org/10.1016/j.cej.2017.09.094
46. I. Amildon Ricardo, C.E.S. Paniagua, V.A.B. Paiva et al., Degradation and initial mechanism pathway of chloramphenicol by photo-Fenton process at circumneutral pH. Chem. Eng. J. **339**, 531–538 (2018). https://doi.org/10.1016/j.cej.2018.01.144
47. B. Gao, W.P. Chen, S.N. Dong et al., Polypyrrole/$ZnIn_2S_4$ composite photocatalyst for enhanced mineralization of chloramphenicol under visible light. J. Photochem. Photobiol. A **349**, 115–123 (2017). https://doi.org/10.1016/j.jphotochem.2017.09.018
48. Y.G. Xu, T. Zhou, S.Q. Huang et al., Preparation of magnetic Ag/AgCl/$CoFe_2O_4$ composites with high photocatalytic and antibacterial ability. RSC Adv. **5**(52), 41475–41483 (2015). https://doi.org/10.1039/c5ra04410c
49. X.M. Zhang, Y. Shu, S.P. Su et al., One-step coagulation to construct durable anti-fouling and antibacterial cellulose film exploiting Ag@AgCl nanoparticle- triggered photo-catalytic degradation. Carbohydr. Polym. **181**, 499–505 (2018). https://doi.org/10.1016/j.carbpol.2017.10.041